Pure and Applied Geophysics

Investigation of Groundwater Occurrences Along the Nile Valley Between South Cairo and Beni Suef, Egypt, Using Geophysical and Geodetic Techniques

Khamis Mansour,[1] M. Gomaa,[1] Ayman I. Taha,[1] Ali M. Radwan,[1] A. El Emam,[1] and Mohamed Rashwan[1]

Abstract— Water is becoming one of the most critical strategic challenges for any country. Egypt has numerous water resources, the most notable being the Nile River. Egypt must seek alternative resources because the development of an Ethiopian dam has reduced the Nile's water flow. Underground water is a source of available water. Therefore, it is necessary to understand the variables governing the flow of subsurface water in Egypt. The primary objective of this study is to examine the hydrological water flow along the Nile Valley between southern Cairo and Beni Suef, Egypt. Applying integrated geophysical and geodetic methods can improve our understanding of the hydrological regime. Fault and stress regimes have a direct effect on underground water flow. Aeromagnetic data were used to determine the main faults in the study area, and four geoelectrical long profiles were measured crossing the Nile Valley. Global navigation satellite system (GNSS) measurements observed along geodetic points covered the study area. The magnetic results show that two faults hit the area, both of which have a pronounced magnetic pattern in the ENE–WSW direction, and two faults in the NW–SE direction. For the geoelectrical results, we observed that the second geoelectrical unit represents the main groundwater aquifer in this region, and it is regulated in the NW–SE direction. The obtained GNSS results demonstrate that compression forces in the south and north influence the hydrological system in the Nile Valley. Faults detected from geological maps and magnetic observations are also influenced by compression forces from the north and south, while the middle section displays tension forces. This geodynamic regime causes the water to flow toward the Nile Valley in the Southwestern of the study regions, whereas water flows outside the Nile Valley in the northeastern part.

Keywords: GNSS, Stress, Strain, Geomagnetic, Geoelectric, Groundwater, South Cairo, Beni Suef.

1. Introduction

Water resource availability has long been a top priority for governments and societies, particularly in places with low rainfall. Due to the ever-increasing population and modernization, the problem of acquiring a sufficient quantity of high-quality water is becoming more urgent. As a result of all of this, surface water cannot be relied upon throughout the year, necessitating the search for additional ways to augment surface water (Alisiobi & Ako, 2012). Many studies have sought to evaluate the groundwater in Egypt. Groundwater storage variations of the Nile Delta basin were studied by Mohamed and Abdelmohsen (2018) and Mohamed (2020) using Gravity Recovery and Climate Experiment (GRACE) data. It was observed that recharge from rainfall was quite low when compared with recharge rates from irrigated agriculture. Over the duration of the study period from 2003 to 2012, the average recharge rate increased due to an increase in artificial withdrawal rates and partial compensation from feeding from the Nile River, returned irrigation flow, and saltwater from the north (Mohamed, 2020). Mohamed (2018) monitored the Nubian Aquifer in Egypt (NAE) and quantified its current recharge and depletion rates, as well as the NAE's interactions with artificial lakes. This was done using the temporal (April 2002–June 2016) terrestrial Water storage (TWSGRACE) data derived from GRACE and other pertinent datasets. The findings show that (1) the observed groundwater loss is primarily caused by persistent base flow recession and/or extreme drought conditions, (2) recharge events only take place when excessive precipitation conditions exist over the Nubian recharge domains and/or when Lake Nasser levels rise significantly, (3) the NAE received a total recharge of 20.27 ± 1.95 km^3 between the years 2004 and 2006 and between 2008 and 2016, and (4) the NAE experienced groundwater depletion of 13.45 ± 0.82

[1] National Research Institute of Astronomy and Geophysics (NRIAG), Cairo, Egypt. E-mail: amradwaneg@yahoo.com

km³/year between 2006 and 2008. Also, many geophysical surveys for groundwater assessment have been carried out in various parts of the world, particularly in dry climates. Khalil et al. (2022) analyzed geomagnetic and gravity data to determine subsurface structural elements for an area (southwestern part of the study area) covering about 485 km² (lat. 29.06–29.25° N and long 30.81–31.03° E); the results revealed that four significant structural forces across the N–S, NW–SE, NE–SW, and E–W directions affected the region and showed that depths to the basement at the region vary between 2.3 and 4.7 km.

Azmy et al. (2021) carried out different geophysical approaches including gravity, magnetic, and electric methods to delineate groundwater and the structural trends in the east of Cairo City (north study area). The gravity and magnetic techniques revealed that different faults dissect the area of trends NE–SW matching the Gulf of Aqaba direction, NW–SE matching the Gulf of Suez, N–S matching the Nile River system, and E–W matching the Mediterranean tectonics. Several authors, including El-Sayed and Mabrouk (1991), have conducted extensive studies of the hydrogeological concepts in the study area. It was determined that the Middle Eocene El Fashn and Qarara formations were the water-bearing formations in the study. These formations were found at depths ranging from 6 to 82 m, with salinity varying between 256 and 5932 mg/l. The transmissivity values observed ranged from 782.5 to 0.55 m²/day, with the variation in transmissivity mainly attributed to the density of fractures (El Abd, 2015). The Beni Suef area gained national attention for exploring groundwater resources despite being part of the unstable shelf, which is known for its thick marine and terrestrial sediments (Said, 1990). However, due to the complex subsurface structure in the area, mapping and characterizing existing groundwater aquifers have proven to be a challenge. The area of study is characterized by the presence of two aquifers, one shallow and one deep. The shallow aquifer is composed of sand and gravel layers, while the deep aquifer is composed of fractured limestone and sandstone layers.

The main goal of our study is to investigate the groundwater resources in the area extending from south Cairo (Helwan and Hykstep towns) to Beni Suef town, Egypt (see Fig. 2), including groundwater flow. From a tectonic perspective, the concerned area is directly adjacent to the beginnings of the Egyptian unstable-shelf zone (Said, 1962). The Beni Suef Basin, a subset of the whole graben system, is surrounded by two NW–SE-bounding faults. Because of the complex structure in the study area, there is a need to integrate geophysical and geodetic studies to evaluate groundwater recharge and water flow. The electrical resistivity method of groundwater research is the most widely used among the numerous geophysical methods for groundwater study (Mohamed et al., 2021; Ariyo, 2011; Olorunfermi, 1999; Mohamed AL Deep et al., 2021) . This is because the field process is simple, the equipment is portable, lower filling pressure is needed, and the penetration depth is greater. In our work, geophysical electric, magnetic, and global navigation satellite system (GNSS) geodetic techniques are applied. The vertical electrical sounding (VES) technique is used to obtain information regarding vertical and horizontal resistivity anomalies in the subsurface geological formation. This is the method applied in the study area for groundwater investigation on both sides of the Nile Valley. Moreover, magnetic measurements are used to study the faults controlling the investigated area. In addition, the integrated interpretation of geodetic and geophysical methods can provide a clear understanding of the geodynamics of the earth and its relation to water flow, so GNSS measurements are observed to calculate the horizontal movements and deformation analysis of the study area. Also, hydrogeological studies of water level changes around the Nile Valley are interpreted.

2. Geologic and Tectonic Setting

The geological complexity of the study region is evident due to significant changes in facies and geologic structures (Fig. 1). Numerous authors have explored the geological setting of the study area and its surroundings, including Abdel-Fattah et al. (2010), Beadnell (1905), Bown and Kraus (1988), Gingerich (1993), Issawi et al. (2009), IWACO (1998), Lotfy and Van der Voo (2007), RIGW (1997; 1998), Said (1962, 1990), Vondra (1974), and Zalat (1995). The
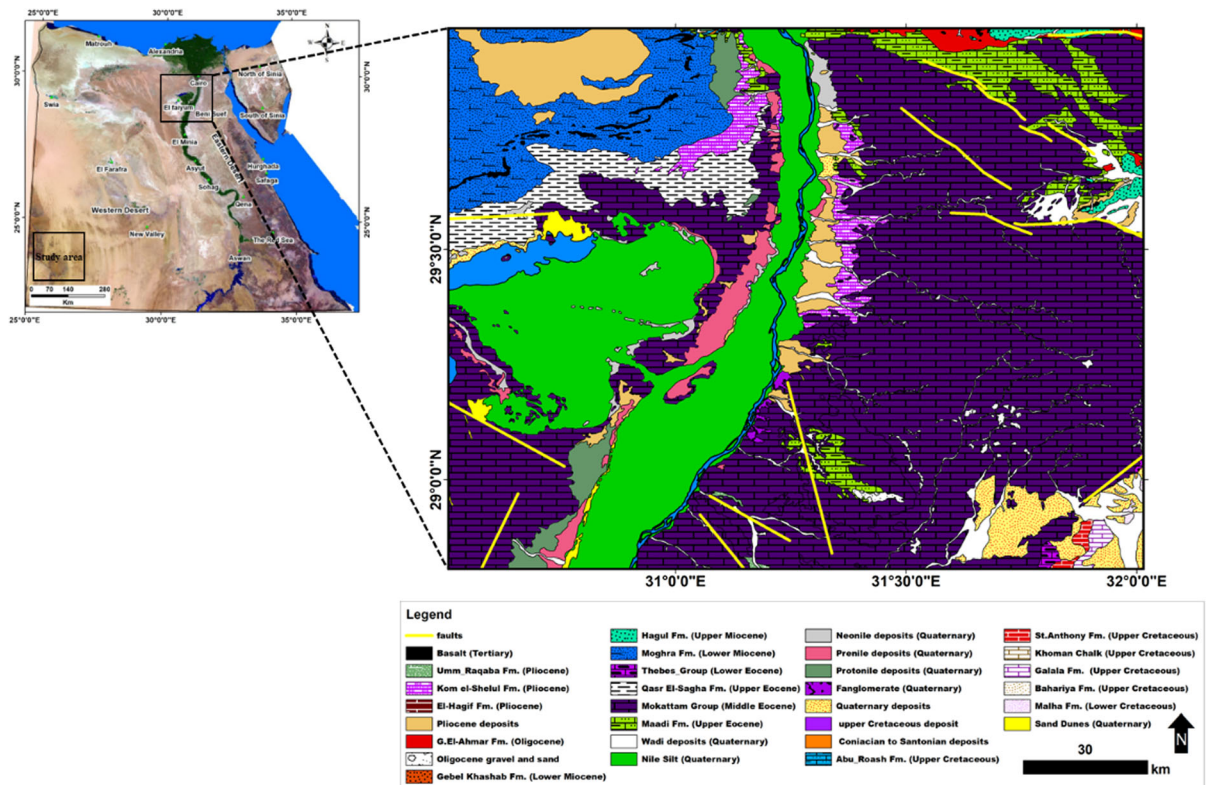
Figure 1
Geological map of the study area based on CONCO/EGPC (1987)

stratigraphic succession covers the Tertiary and Quaternary periods (Fig. 1).

Holocene and Pleistocene Quaternary deposits are differentiated based on their characteristics. The Holocene sediments include aeolian deposits, young lacustrine deposits, and young Nilotic deposits. The aeolian deposits consist of loose quartz sand, while the young lacustrine deposits are composed of fine sand and clay with thin residues of gypsum and carbonate minerals, and are found in the El Fayoum depression. The young Nilotic deposits, which vary in thickness from 1 to 12 m, consist of silt and fine sand, mainly by quartz grains and heavy minerals, because of the yearly Nile floods. Old lacustrine and old Nilotic deposits are two types of Pleistocene deposits. Old lacustrine sediments (45 m thick) are visible in the form of terraces at levels +43 m, +30 m, and +25 m, indicating a Pleistocene freshwater lake fed by the Nile. Old Nilotic deposits (190 m thick) consist of sand and gravels that form a strong

groundwater aquifer and are located at the Nile–Fayoum division. The deposition of Pliocene, Miocene, Oligocene, and Eocene rocks is observed. The Pliocene layers are characterized by fossiliferous sandstone and are typically underlain by Quaternary sand and gravels, as observed in certain locations in the Nile–Fayoum split (Said, 1962). The Late Pliocene El Hagif Formation is composed of a smoky white nonfossiliferous limestone with marl interbeds (Araffa et al., 2021). To the north of the El Fayoum depression, Miocene rocks can be found in the form of overlying basalt exposures in Gebel Qatrani. These rocks are composed of alternating sand and gravel beds, as well as silicified timber remnants. The Lower Miocene deposits in the study region are represented by the Moghra Formation, which consists of fluviomarine sediments (Said, 1962). Below the Miocene rocks in the Gebel Qatrani region are Oligocene rocks that are covered by a basalt sheet. These rocks are composed of sand and sandstone with

interbeds of shale and marl and are rich in silicified timber and terrestrial animals.

Eocene rocks, which are widely distributed in the El Fayoum-Wadi El Rayan and East Nile sectors, are the earliest exposed rocks in the region. They are 390 m thick and divided into Upper and Middle Eocene rocks. The Upper Eocene rocks, namely the Qasr El Sagha and Birket Qarun formations, are concentrated at the northern limits of the cropped land bordering Qarun Lake and the hill block of Garet Gehannam on the west side of the El Fayoum valley (Beadnell, 1905). Middle Eocene rocks, on the other hand, are composed of limestone and marl with shale intercalations. The Mokattam Formation, which dates from the Middle to Upper Eocene, is a succession of sedimentary carbonates and less prevalent clayey rocks. It is divided into four units, namely the carbonate, clastic, lower carbonate, and lower clastic units (Aly et al., 2020). The Maadi Formation consists of a series of fossiliferous and sandy limestone strata, while the major components of the Thebes Formation are chalky limestone and chalk with chert nodules. These carbonate rocks have undergone diagenetic phenomena such as karstification, dolomitization, and dissolution.

The Upper Cretaceous succession includes the Khoman Chalk and St. Anthony formations, which are composed of chalky limestones, marls, and sandstones. The homogeneous chalky limestone of the Khoman Formation varies with the interbedded limestone and shale of the Abu Roash Formation. The lower Cretaceous Succession includes the Galala, Baharyia, and Malha formations, which consist of clastic deposits of shallow marine sediments of sandy shale intercalations with limestone interbed.

The area under study can be considered a petroliferous fracture basin. Shehata et al. (2018) showed that the upper and lower constituents of the Kharita Formation are shaped between the syn–rift stage of basin formation. Moreover, the studied basin is defined as a half-graben rift basin due to tensional forces that occurred in the central and northern parts of Africa during the expansion of the South Atlantic Ocean in the Early Cretaceous age as revealed by Bosworth et al. (2008). This basin is one of the features of intracontinental rift basins (Bosworth et al., 2008). In accord with Moustafa (2008), the Jurassic

and early stage of Cretaceous sediments was stored in half-graben basins as the North African rifting basins. During the Early Cretaceous time, continental rifting at North Africa and Arabia was very dynamic, and structures associated with the two tectonic regimes such as horsts, normal fault propagation folds, and strike slip-related anticlines formulated the main structural traps in the study area (Guiraud & Bosworth, 1999).

3. Data and Methodology

The various geological structures in the study region were evaluated using aeromagnetic data. The total magnetic anomaly map, scale 1:100,000, is a well-expressed magnetic anomaly map of the study zone. This map was prepared and compiled by Getech (1992), after removing the regional magnetic trend. Reduction to the pole (RTP) was estimated using the mean values of inclinations and declinations (I=43°, D=4.1°) for each locality in Egypt, and then a reasonable map for interpretation was created. Using the analytical signal, magnetic interpretation was performed, 2D radially averaged power spectrum, Euler deconvolution, and 2.5-D magnetic modeling methods. In addition, for covering the study area, 43 VESs were measured by a Schlumberger array using SAS 1000 in the west and east side parts of the Nile Valley at the study area. Furthermore, steps from 1 m until reaching 1000 m (AB/2) were applied in VESs. By using (Interpex-IX1DV4) software for resistivity data processing and interpretation, very long geoelectric cross sections have been represented from these 1D VESs (Fig. 2).

3.1. GNSS Observations

GNSS geodetic measurements have been used to model the horizontal movements along the study area. Permanent GNSS stations at Katamayia, Cairo (KATA) and Helwan, Cairo (PHLW) were used from 2013 to 2020, and the daily solution was estimated. Permanent stations have continuous GNSS observations. In addition, campaigns at stations Pyramids, Giza (PYRA), Hyksteb, Cairo (HYKS), Elsaf, Giza
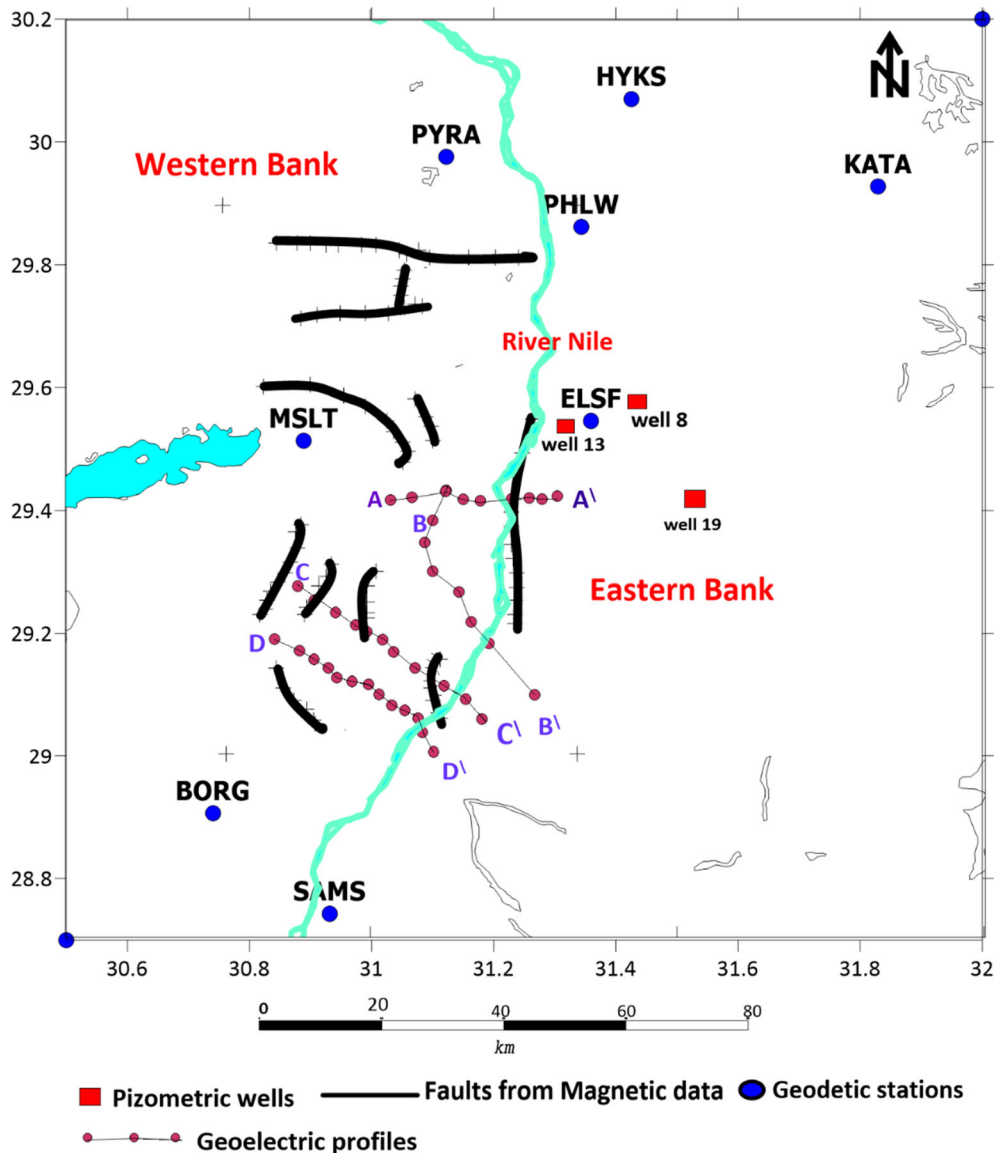
Figure 2
Site map showing geophysical and geodetic surveys

(ELSF), Mesalat, Fayoum (MSLT), West Beni Suef (BORG), and East Beni Suef (SAMS) from 2007 to 2009 were observed to obtain an overview about the geodynamics of the area under investigation. Nowadays, the accuracy of GNSS observations reaches the submillimeter level. A distinct and consistent reference system must be employed throughout all phases of the data processing for coordinate determination in order to identify the station locations and velocities of the monitoring network. A stable origin is required for velocities, and position coordinates must belong to a coherently specified coordinate system. A reference frame, which is a collection of reference stations with coordinates in accordance with the description of the reference system, serves as the practical implementation of the reference system. The user receives the reference frame via ephemeris, station coordinates, and related products. The

coordinates of the stations in relation to the satellite orbits vary over time due to crustal deformation (movements of tectonic plates and territorial deformations). As a result, during data processing, we must convert the coordinates of the reference frame using the velocities at the observation epoch. A dense spacing is required in the measuring area and the reference system for the ground stations and satellites coordinates must be the same. Only the International Terrestrial Reference System (ITRF) can achieve this. In our paper, ITRF2014 has been used as a reference frame for GNSS observations. The advanced scientific software Bernese (V.52) (Dach et. al., 2007) has been used in processing GNSS data. Models, products, and processes can be used to describe the GNSS data processing approach. Antenna phase center variation, ionospheric and tropospheric models, ocean tide loading, ambiguity resolution approach, cut-off angle, and datum have been defined during the processing stage. These definitions and models are necessary for the final products, which include station coordinates and velocities. Daily solutions for all stations were processed and the final combined solution was produced using the ADDNEQ program in Bernese. Horizontal velocities were calculated in the final stage of processing of the combined solution. Moreover, estimating crustal stresses or strain rates from discrete geodetic observations is a common requirement in geophysical studies. Angle variations between stations, baseline line length changes, and/or station displacements can all be used to measure horizontal strain. When the changes are split by the time range over which the changes occur, strain rates are calculated. In our study, we used horizontal velocities to determine the strain tensor parameters and principal strain axes.

For calculation of strain parameters, the station displacements, baseline line length changes, or angle changes between stations can all be used as data to estimate horizontal strain. Strain rates are calculated by dividing the changes by the time span of changes. A modified least squares approach was presented by Shen et al. (2015) to model stresses as continuous functions.

To ensure solution continuity, this technique iterates through a 2D space with arbitrary very small increments. The horizontal velocity field is expanded to its first-order derivatives or is represented by a model of rigid block motion (translation and rotation) and a homogeneous strain field, at each interpolation coordinate R. The deformation parameters are then connected to the displacement data via a linear relationship:

$$d = Am + \mathcal{E}$$

where d is the data vector; m is the vector for the unknowns of translation, rotation, and strain; A is the partial derivative matrix; and $\mathcal{E}$ is the error vector.

In the current study, the strain parameters have been calculated using the Strain Tool developed by Shen et al., 2015. Using a set of data points and tectonic velocities on the earth's crust, the software program Strain Tool can estimate and calculate the parameters of the strain tensor. This utility is composed of three main components: the main executable (StrainTensor.py), a Python module named by strain, and a set of shell scripts for plotting StrainTensor.py (Shen et al., 2015).

4. Results and discussion

The RTP magnetic anomaly map (Fig. 3b) shows the real location of the sources causing the magnetic anomalies based on aeromagnetic data. The presence of faults that split the study region into three blocks with magnetization variations is shown by the alternating higher and lower anomalies. Magnetic signals are clear and powerful when the basement rocks are heterogeneous and deformed. From the magnetic results, two faults influence the area, with their most common magnetic trend impacting in the ENE–WSW line, and two faults in the NW–SE position, as shown in (Fig. 3b). The average depth levels to magnetic anomaly sources in the study area were computed using the 2D radially averaged power spectrum approach, as shown in Fig. 4, using the Geosoft package. The resultant radially averaged power spectrum diagrams (Fig. 4) show that the shallower, middle, and deeper magnetic sources have average depth levels of around 300, 900, and 2800 m, respectively.
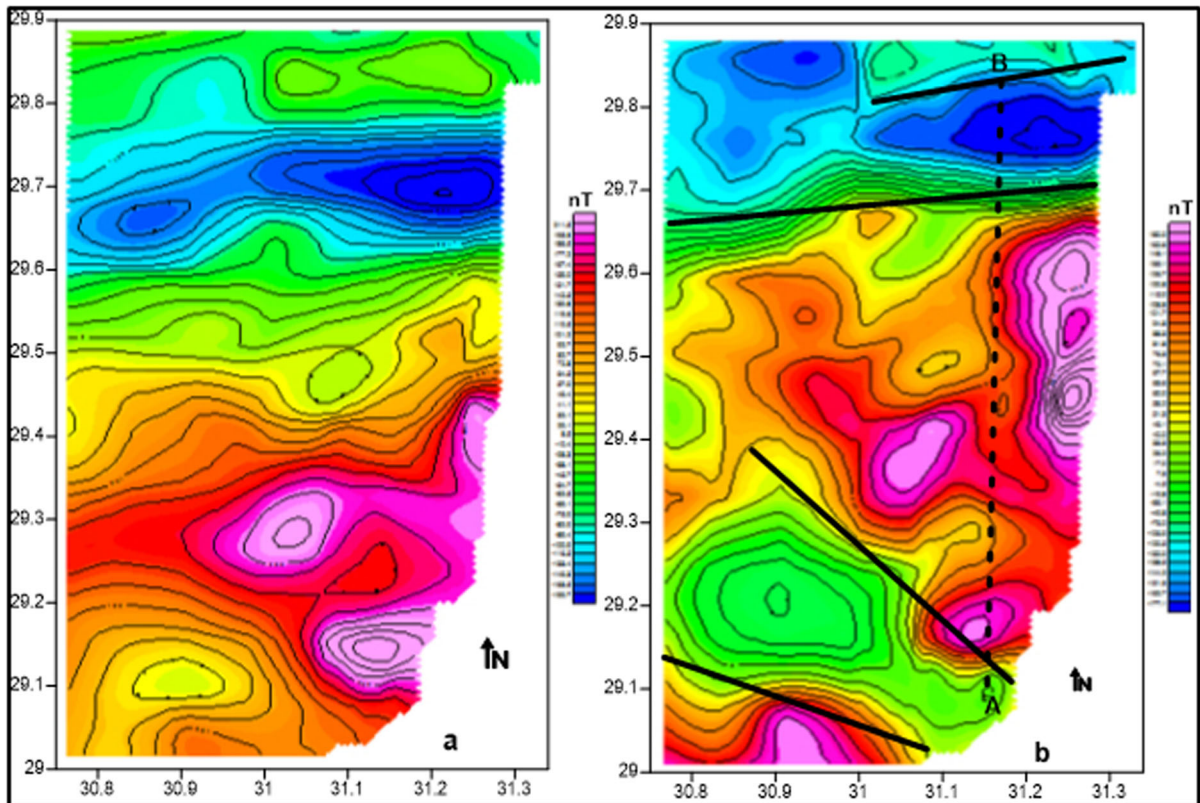
Figure 3
a Magnetic map of total intensity. **b** Magnetic anomaly map of RTP

The RTP magnetic data were used to calculate the depths of magnetic sources based on the gradients of x, y, and z (dT/dx, dT/dy, and dT/dz), using the 3D signal analytical technique. Geosoft was used to create the analytical signal map (Fig. 5a). It shows many circular and linear maximum closures in the study region, which relate to the origin of underground magnetic bodies. In addition, the analytical signal map may be utilized to calculate the estimated source body depths in accordance with the measurement level. According to our data, the depth varies from 1.3 km to around 3 km. The Euler solutions were derived using Geosoft with a structural index (SI) of zero and a 10×10 km window size. The Euler plots (Fig. 5b) display accurate linear and sigmoidal Euler anomalies that describe the source's trend, depth, and position. The depth of the Euler anomalies range from 1 to 2.5 km. The Euler plot's linear clusters demonstrate the expansion of the

predicted linear step of different magnetic susceptibility differences attributable to faulting at various depths. The length and extent of these linear Euler anomalies vary.

The magnetic anomaly profile was also subjected to 2D modeling. The predicted magnetic susceptibility for the subsurface basement rocks was 0.005 (SI units) and zero for the nonmagnetic sedimentary layer. The form of the basement surface may be shown in the interpreted cross section following the profile of magnetic anomaly (AB), which extends north–south (Fig. 6). The minimum and maximum depth values to the basement surface are 0.8 and 3.8 km, respectively, as shown in Fig. 6.

Using the IX1D program, DC resistivity data were interpreted quantitatively to identify the true resistivity and subsurface layer thickness (Interpex, 2008). Figure 7 shows the field curves of resistivity data from different localities in the study area. In Fig. 7A,

RADIALLY AVERAGED POWER SPECTRUM

DEPTH ESTIMATE
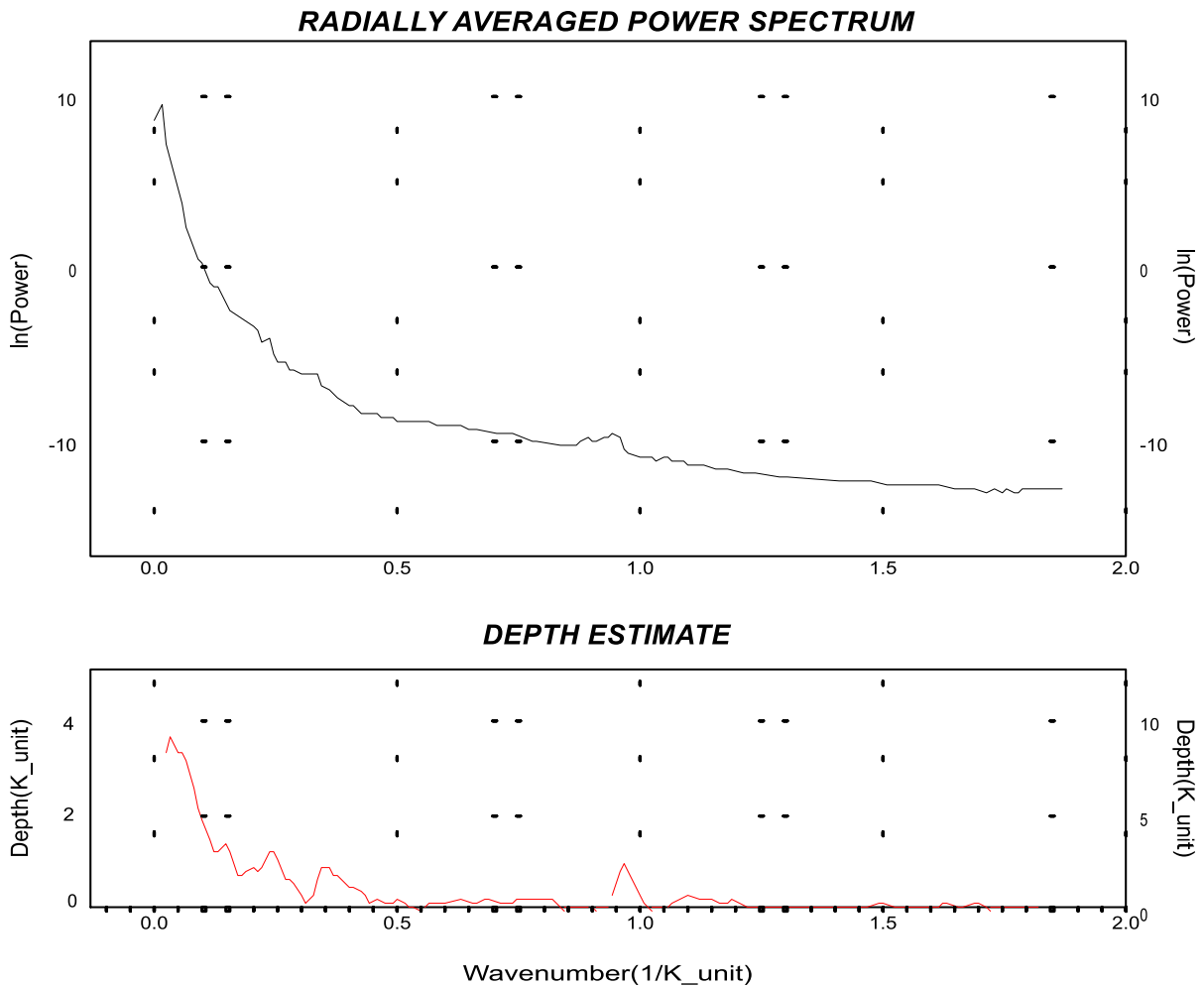
Wavenumber(1/K_unit)

Figure 4
2D power spectrum with radial average

field curves for several VESs found in the western part of the study area, VESs 10 and 12 begin with resistivity values of 330 and 2077 ohm.m, respectively, while other VESs begin with very low resistivity values varying from 3.4 to 28 ohm.m. The most noticeable resistivity values vary from 1 to 10 ohm.m, with a mean value of 3.5 ohm.m. Figure 7B presents apparent curves for some VESs west and east of the Nile River, with resistivity values varying from 1 to 100 ohm.m and an average value of 14 ohm.m, whereas Fig. 7C demonstrates apparent resistivity curves for a few VESs on the east side of the Nile River, with resistivity values ranging from 2.2 to 670 ohm.m and an average value of 225

ohm.m. Around the Nile River, resistivity values increase from low to high and then back to low with depth, whereas on the eastern side, resistivity values begin at high levels and decrease gradually with depth.

An example of 1D inversion steps for VES number (28) data is shown in Fig. 8, with the approach degree between apparent resistivity data and smoothed theoretical curve (Fig. 8A), the field curve with a smooth multilayer resistivity inversion model (Fig. 8B), and the final inversion step with the best approach between field curve and theoretical curve with the lowest root mean square error value (Fig. 8C).
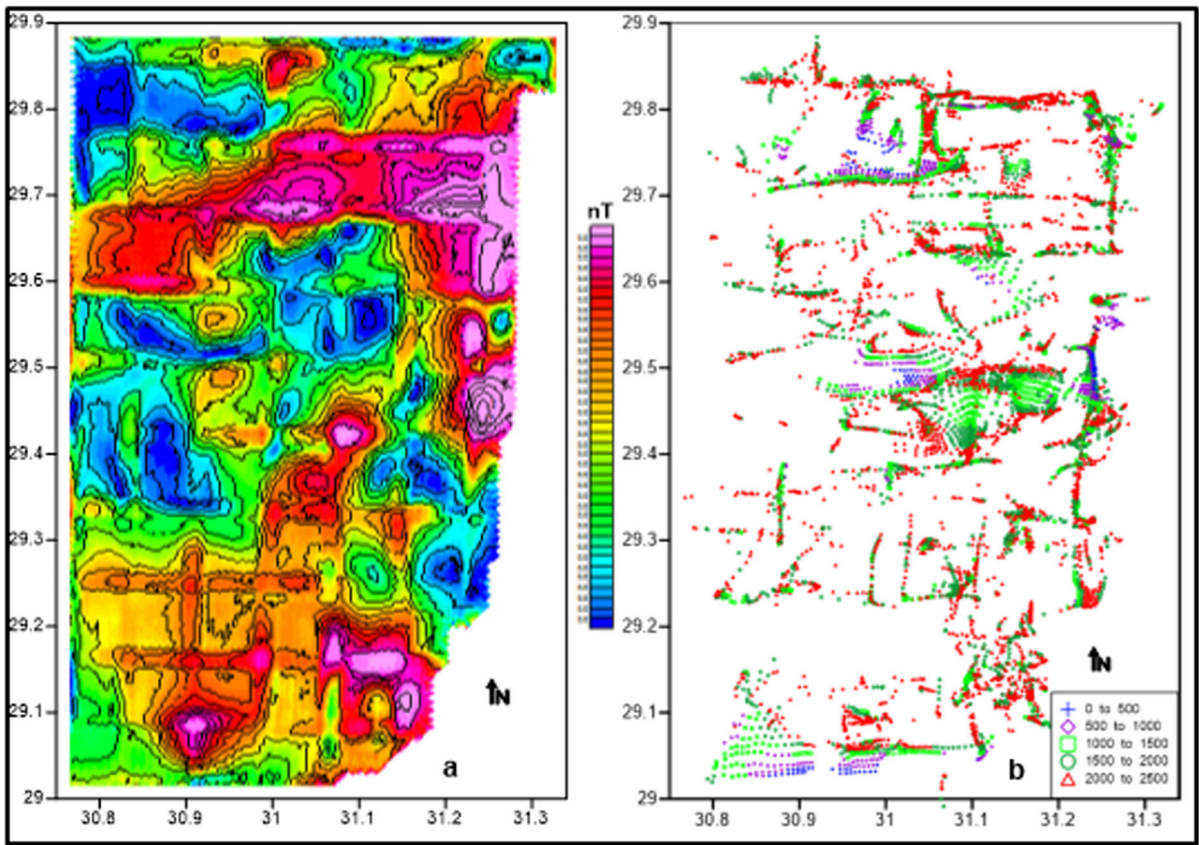
Figure 5
a Three-dimensional analytical signal map. **b** Application of Euler deconvolution on the aeromagnetic data
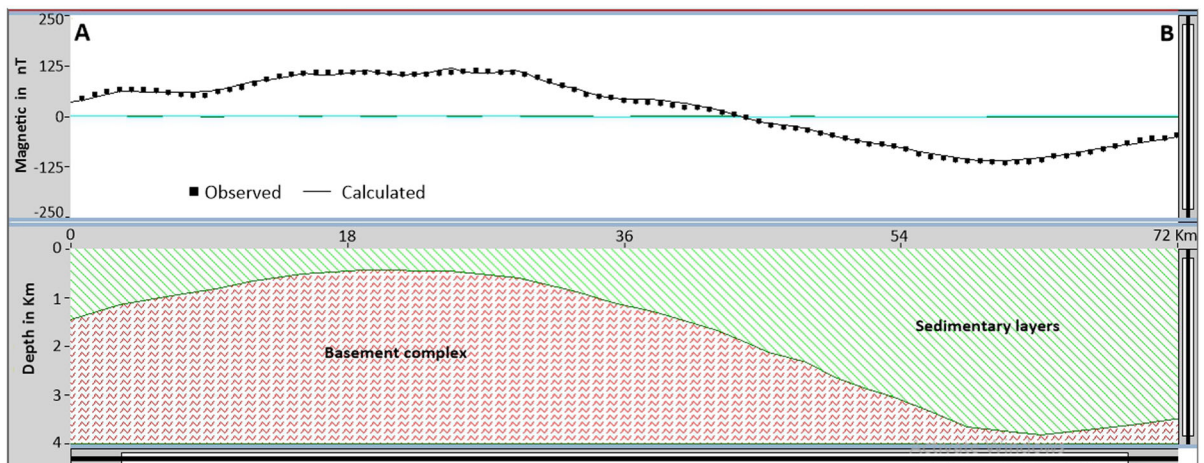

Figure 6
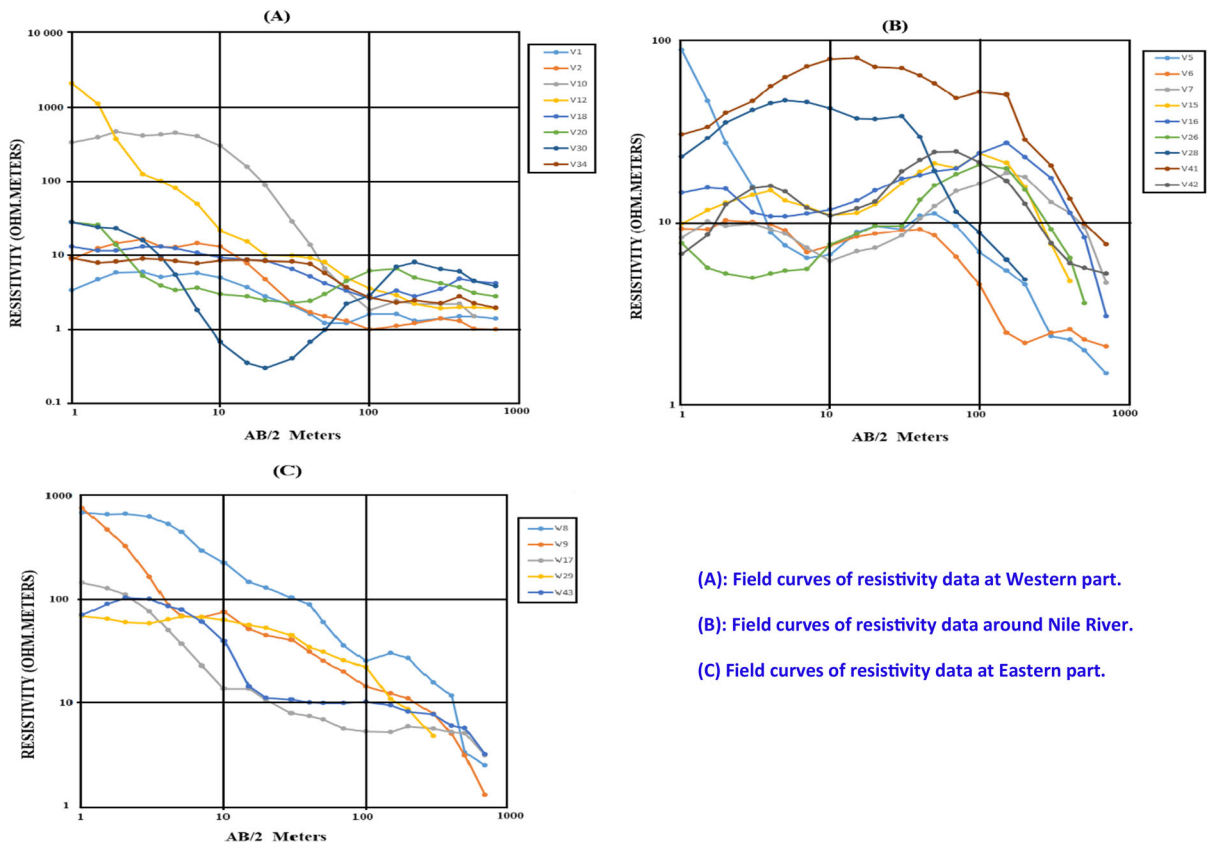Two-dimensional model along magnetic profile AB

Figure 7
Samples from resistivity field curves in the study area

Table 1 presents the quantitative interpretation results of a selection of VESs in the study region, where the resistivity of the first layer varies between 2.4 and 734 ohm.m with thickness ranging from 0.3 to 3.56 m and a mean value of 1.2 m, while the resistivity of the second layer varies between 38 and 208 ohm.m with thickness ranging from 0.88 to 19 m and a mean value of 5 m. In general, the surface and near-surface dry layers are reflected by the first and second geoelectrical layers and can be named the first unit. In some locations, the third one characterized by extremely low resistivity values "may be interpreted as a clay and/or marl layer," whereas in others, the VESs indicate a water-bearing deposit, part of a water-bearing formation.

The low resistivity values at this stratum imply an increase in clay and/or marl content. The fifth layer found in all VESs in some cases appears as the last layer. Its resistivity ranges from 0.62 ohm.m to 38.3 ohm.m with a mean value of 5.64 ohm.m, and its mean thickness is 117 m (part of water-bearing formation). In general, the sixth layer is associated with a very low resistivity value. The bottom layer exhibits extremely low resistivity values compared to the shale and/or marly limestone layer, and it extends to the end of the depths investigated. The water-bearing layers are shaded in green in Table 1.

Generally, geoelectrical sections extended from west to east and NW to SE as shown in Figs. 2 and 9. The geoelectrical layers, along with detected wells of groundwater, are all represented in the geoelectrical cross sections to highlight the groundwater thickness, potentiality, and extension of the water-bearing strata. The subsurface characteristics of the study area which are viewed in four geoelectric cross sections are calibrated with available data. The subsurface

VES 28
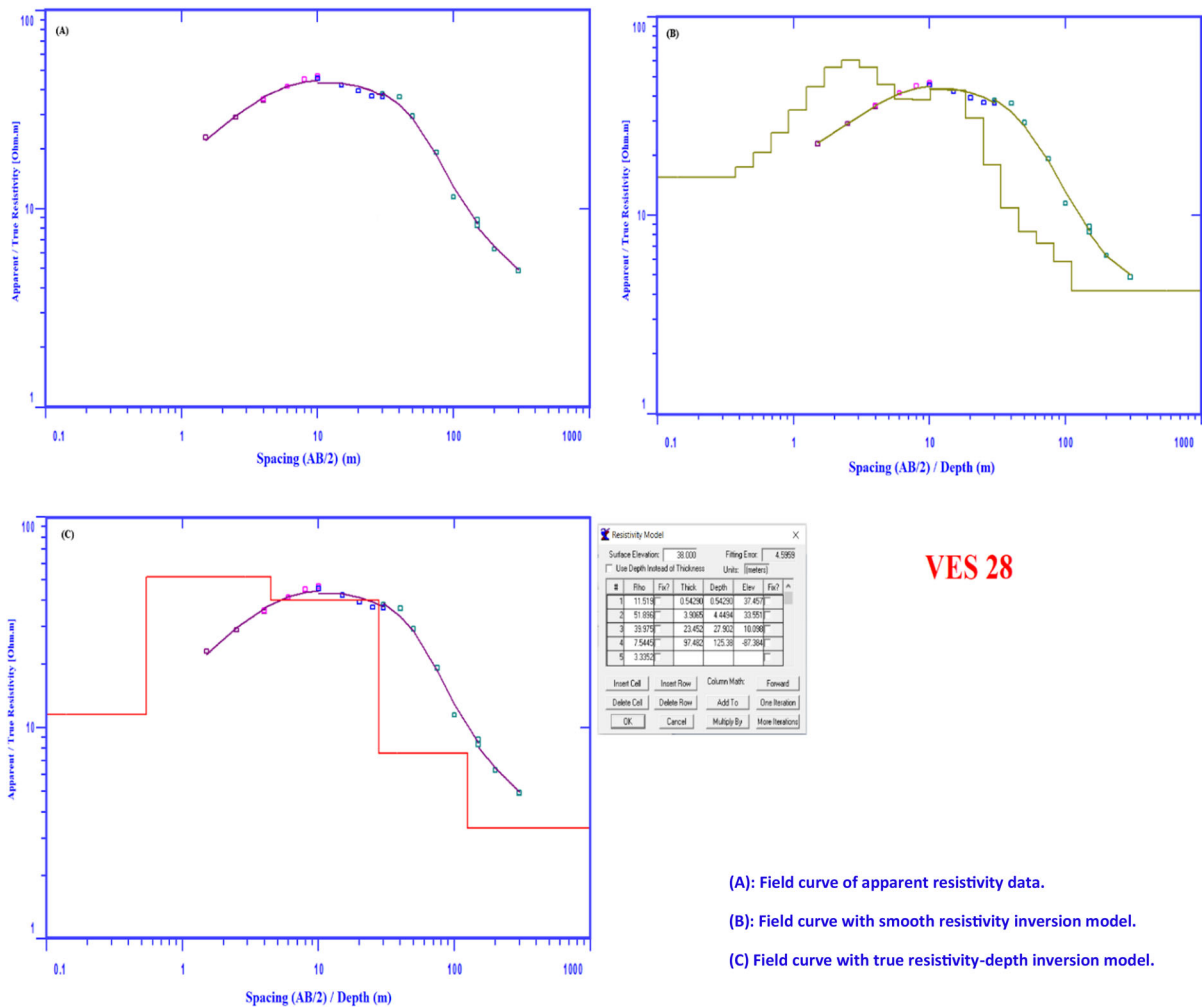
(A): Field curve of apparent resistivity data.

(B): Field curve with smooth resistivity inversion model.

(C) Field curve with true resistivity-depth inversion model.

Figure 8
Processing steps for samples from resistivity field curves in the study area

geoelectric sequence of the study area is identified and grouped into four geological units with different thicknesses and resistivity. The geological units differ depending on the rock formation and the amount of water (Table 1). These units are described as follows:

The first layer contains gravel, mud, and loose sand from recent deposits (dry layer). The second unit contains sand of various sizes (coarse sand, medium and fine) with intercalations of clay, and it represents the main groundwater aquifer in the study area in particular around the Nile River (Nile Valley). The third layer is composed of clayey sand and/or silty clay, marl, and limestone with intercalations from thin layers of very fine sand (saturated layer). The last

layer has very low resistivity values and is composed of shale/clay and/or marly limestone sediments. The water content of the saturated zone has relatively high resistivity values around the Nile River and the eastern part of the study area, while in the western part the resistivity values are low. The resistivity of these layers is affected by the type of water-bearing formation and salinity of the water. The thickness of the water-bearing formation is controlled by the geological structure, as the thickness is greater in the eastern part than the western part, with the presence of fault sets acting as a seal for water flow to the west. The main rock units in the western part are clay and/or shale with thin layers of sand and/or silt. The solid
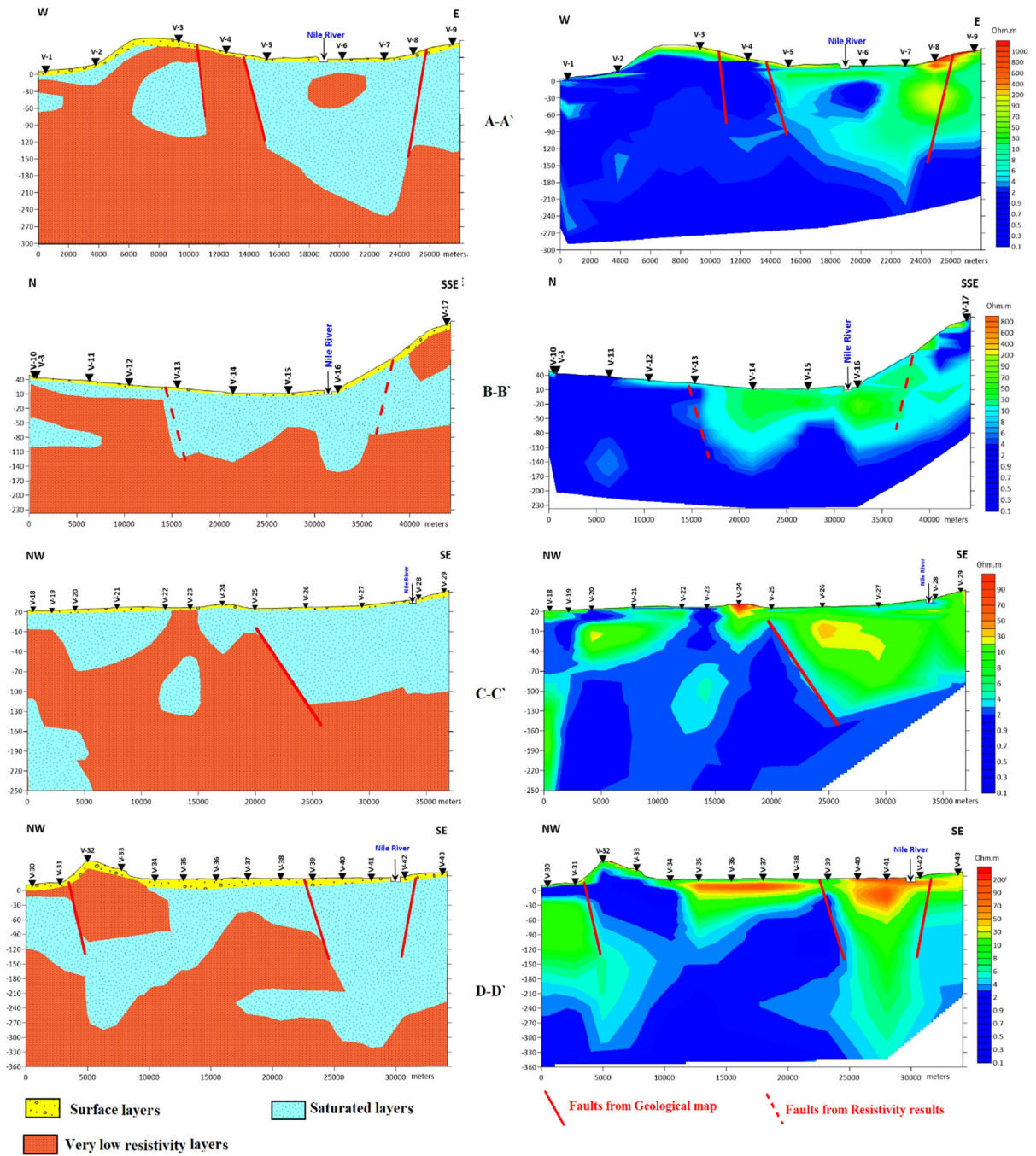
Figure 9
Geoelectric sections A–A′, B–B′, C–C′ and D–D′. The faults from the geological map and estimated faults from resistivity data. Different layers estimated from true resistivity values

fault lines (Fig. 9) are from the geological map, while the dashed fault lines are estimated from resistivity results.

4.1. GNSS results

From GNSS observations, we obtained regional horizontal movements which represent the plate

Table 1

Summarized results of some VESs in the study area

V No.		First layer	Second layer	Third layer	Fourth layer	Fifth layer	Sixth layer	Seventh layer	Note
1	Res	2.6510	3.7950	0.48327	3.5506	0.83213	1.5768		Western part
	Thick	1.0118	9.3438	18.374	37.152	70.765			
2	Res	2.3928	25.052	0.75127	2.6378	0.79811	2.4643		
	Thick	0.57414	4.1177	9.3710	17.526	51.617	157.03	0.51081	
3	Res	154.75	49.194	0.57259	4.0536	1.2098			
	Thick	3.5681	8.1836	17.739	83.830				
18	Res	13.350	8.9979	2.3732	14.075	1.8829			
	Thick	3.1670	16.225	123.47	135.59				
19	Res	20.141	2.7172	0.84965	14.204	1.2793	4.1602		
	Thick	0.77209	5.8242	11.944	71.379	192.75			
24	Res	151.69	39.866	110.20	10.097	1.8171	2.2042		
	Thick	0.41185	0.88102	14.942	57.928	208.52			
35	Res	266.22	8.8149	2.2957	7.6226	1.8250			
	Thick	2.1055	19.361	147.78	369.79				
5	Res	130.63	7.5367	17.227	2.5933	0.87867			Around Nile River zone
	Thick	0.54300	9.5298	42.713	258.66				
6	Res	10.234	18.629	4.4015	24.684	0.88047	4.9503	0.86431	
	Thick	0.86664	1.9005	4.6876	16.170	50.054	171.07		
15	Res	6.6341	20.692	5.0901	28.749	0.61699			
	Thick	0.57260	1.8806	5.4310	78.788				
16	Res	16.206	12.524	27.265	64.316	7.5648	1.1837		
	Thick	2.5745	5.1780	28.892	67.808	68.014			
26	Res	11.324	6.4730	10.998	25.345	2.0668			
	Thick	0.46512	3.5750	14.228	86.854				
28	Res	11.519	51.896	39.97	7.5445	3.3352			
	Thick	0.54290	3.9065	23.452	97.482				
41	Res	34.788	208.05	65.687	92.357	11.233	5.1579		
	Thick	1.3648	5.1889	12.525	61.985	220.18			
42	Res	2.9668	56.263	3.3919	52.624	8.3883	5.0514		
	Thick	0.33516	0.91489	3.4076	26.860	87.457			
9	Res	734.42	29.628	108.50	34.993	13.000	0.60519		Eastern part
	Thick	0.91041	1.3160	4.1546	17.561	167.08			
17	Res	325.92	23.871	2.7226	11.181	2.3071	10.928	1.6874	
	Thick	1.4446	9.2891	10.496	16.730	72.688	117.17		
29	Res	71.400	38.690	99.894	22.189	38.291	4.6364		
	Thick	1.5884	1.9702	8.2187	18.377	47.732			
43	Res	55.608	124.09	6.0282	13.385	9.0120	2.3852		
	Thick	0.36681	2.8831	8.0643	25.305	174.94			

motion of the Nubian plate with average velocity of 18 mm/year northward and 23 mm/year eastward. The accuracy of the estimated regional velocities is 0.5 mm. To obtain an accurate view regarding the local movement in the study area, we have to remove the regional effect of plate motion. The Euler pole calculated by Altamimi et al. (2017) was used to verify the local movement. According to Euler's fixed-point theorem, any motion of a rigid body on a sphere's surface may be described as a rotation about a suitable rotation pole, known as a Euler pole. This theorem has been utilized by geologists to understand the movements of tectonic plates. The direction of motion and the border orientation both affect what happens at a boundary between two plates. Subduction, spreading, and strike-slip motion are all present in Euler pole theory. The Global Positioning System satellites and other space geodetic methods, such as Very Long Baseline Radio Interferometry, can be used to observe these motions in the real world. By using the parameters of the Euler pole calculated for the Nubian plate, the local movements have been
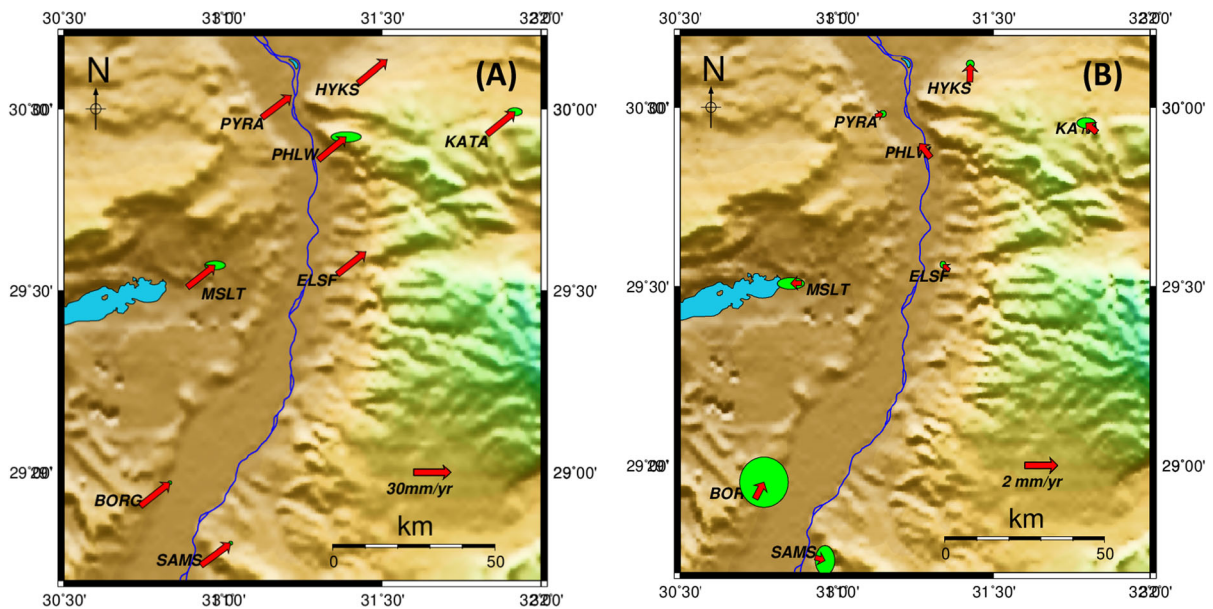
Figure 10
A Regional horizontal movements per year, **B** local horizontal movements per year

Table 2

Values of horizontal velocities in meters (Ve = velocity eastward, Vn = velocity northward)

Points	Regional Ve (m)	Regional Vn (m)	Local Vn (m)	Local Ve (m)
BORG	0.0238	0.0189	0.001	0.0005
ELSF	0.0229	0.0181	0.0003	−0.0003
HYKS	0.0232	0.0188	0.001	0.00002
KATA	0.0226	0.0183	0.0005	−0.0006
MSLT	0.0225	0.0178	−0.00003	−0.0006
PHLW	0.0225	0.0186	0.0008	−0.0006
PYRA	0.0236	0.0179	0.0001	0.0004
SAMS	0.0239	0.0176	−0.0001	0.0006

estimated after removing the Euler pole parameters of the plate. Therefore, we subtract the values of Euler pole motion from the estimated regional velocities. The local movements vary between 0.5 and 1.1 mm/year to the north and 0.6 mm/year to the east. The accuracy of the estimated regional velocities is 0.1 mm. Maximum local horizontal velocities found in HYKS station are about 1.1 mm per year. Also, the central area gives the lowest velocities (see Fig. 10A, B). Values of local movements are shown in Table 2.

From a geodynamics perspective, the maximum shear strain (Fig. 11A) shows that the central area has a low deformation rate (from 2 to 10 nano-strain per year), in contrast to the northern and southern regions, which demonstrates significant deformation (about 40 nano-strain per year). Faults deduced from magnetic observations are affected by the compression forces coming from the north and south. In addition, there is a direct effect on the underground water level change which gradually increases from east to west toward the Nile Valley, affected by the high deformation coming from the north and south. Therefore, the geodynamics support the hydrological view.

In the western bank of the Nile Valley, the piezometric surface was studied between 1990 and 2006. Groundwater flows in two directions in the study area: one from the southwest to the Nile River in the southern half, and the other from the Nile River to the northwestern part in the northern part. It can be concluded that the Nile River is an influent river (gained) in the southern portion, but an effluent stream in the northern part. From the principal strain axes, it can be observed that the south area exhibits stretching in the southwest. This stretching allows the
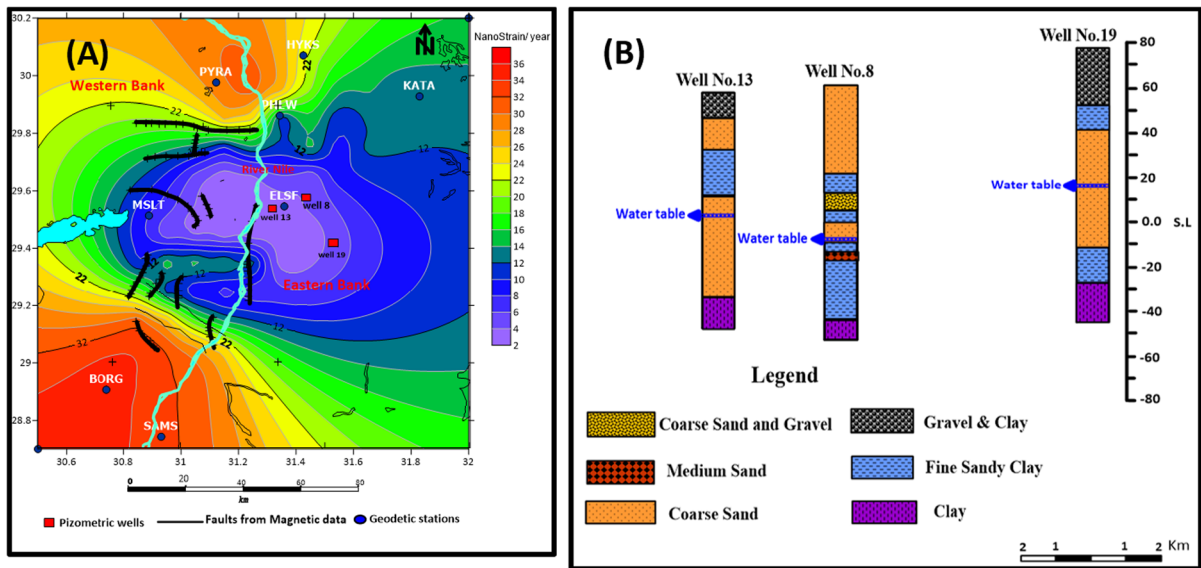
Figure 11
A Maximum shear strain per year and **B** lithological sequence of wells in the area east El Saff (Plio-Pleistocene aquifer)

water to flow toward the Nile Valley. In contrast, the principal strain axes in the north show opposite directions, represented by compression, forcing the water to flow outward to the Nile Valley (see Fig. 12).

5. Discussion and Conclusion

This study was conducted to investigate the underground water and deformation control of the water flow (from South Cairo to Beni Suef, Egypt). To achieve the proposed aim, integrated geophysical and geodetic methods were used. Magnetic, geo-electric, and GNSS measurements were observed covering the study area. Analytical signal, 2D radi-ally averaged power spectrum, Euler deconvolution, and 2.5-D magnetic modeling methods were used for magnetic interpretation. We found that the area is impacted by two fault trends, one in the ENE–WSW direction and the other in the NW–SE direction, with the most common magnetic trend in the ENE–WSW direction. The depth of the basement rocks varies between 0.8 and 2.5 km.

The interpretation of magnetic data indicates deep faults, while faults deduced from geoelectric profiles represent shallow faults. In some cases, the shallow faults extended deeply as in profile C–C′. In this profile, the fault between VES 24–25 is shown in both geoelectric and magnetic data in Fig. 2. The geoelectric method shows that near the Nile River and the eastern area of the study region, the water content of the saturated zone produces unusually high resistivity values, while low resistivity values are found in the western region. The type of water-bearing formation and water salinity have an impact on the resistivity of these layers. The geological structure is the main reason for the greater thickness of water-bearing formation in the east than in the west. Also, the presence of fault sets acts as a seal for water flow in the western direction, and the thickness of the water-bearing formation is regulated by this structure. The main rock sections in the western region are composed primarily of clay and/or shale, with a few minor layers of sand and/or silt. In addi-tion to the main structure of the Nile Valley, most of the faults were found in the western part. The western north faults have E–W trends.

On the other hand, faults in the Southwestern show N–S directions. The different structural behavior from north to south introduces a compli-cated deformation regime. The deformation in the
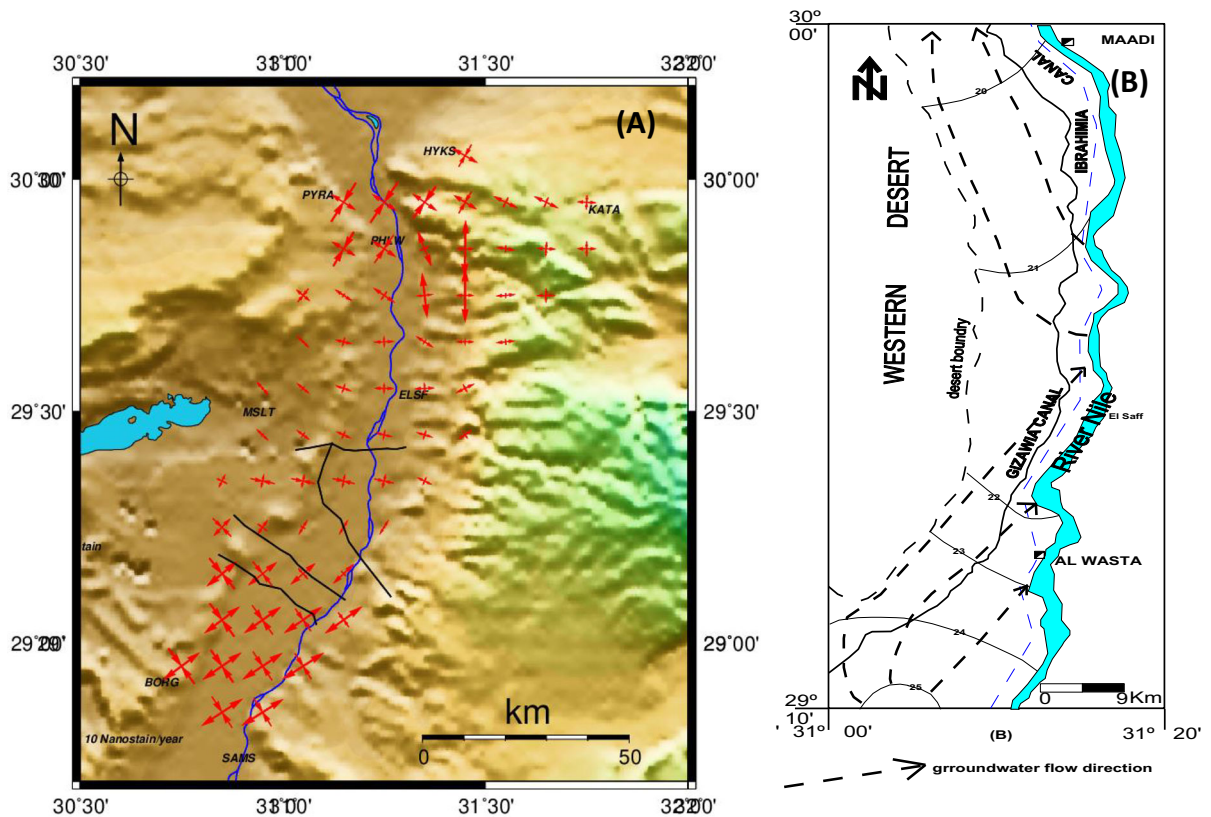
Figure 12
A The principal strain axes and **B** piezometric surface map of the Quaternary aquifer in southern Giza

western north indicates compression, while the Southwestern part shows extension. The groundwater potential increases in the Nile Valley (around the Nile main stream) and on the eastern side, while it decreases in the western part. From GNSS results, the plate motion of the point related to the Nubian plate reaches 23 mm eastward and 18 mm northward. Moreover, the local movements reach 1 mm to the north and 0.6 mm to the east. GNSS measurements show significant shear strain values in the north and south of the area reaching 40 nano-strain per year. The crustal deformation controls the water flow toward the Nile Valley in the Southwestern and outward toward the Nile Valley in the western north. Based on our study, integrated tools are essential for any study of underground water flow.

Our study represents an attempt to improve the knowledge regarding the water flow properties and factors controlling this flow using the available recent

and advanced geophysical and geodetic tools. However, it is recommended to extend the geoelectric profiles and GNSS observations to cover more areas in Egypt in the search for groundwater.

Declarations

Conflict of interest The authors declare that they have no known competing financial interests or personal relationships

which have or could be perceived to have influenced the work reported in this article.

Open Access This article is licensed under a Creative Commons Attribution 4.0 International License, which permits use, sharing, adaptation, distribution and reproduction in any medium or format, as long as you give appropriate credit to the original author(s) and the source, provide a link to the Creative Commons licence, and indicate if changes were made. The images or other third party material in this article are included in the article's Creative Commons licence, unless indicated otherwise in a credit line to the material. If material is not included in the article's Creative Commons licence and your intended use is not permitted by statutory regulation or exceeds the permitted use, you will need to obtain permission directly from the copyright holder. To view a copy of this licence, visit http://creativecommons.org/licenses/by/4.0/.

Publisher's Note Springer Nature remains neutral with regard to jurisdictional claims in published maps and institutional affiliations.

REFERENCES

Abd, E. S. E. (2015). Hydrogeological study of the groundwater aquifers in the reclamation area of the desert fringes east Nile between Biba—el Fashn, Eastern Desert Egypt. *Egypt Journal Pure Applied Sciences, 53–4*, 13–25.

Abdel-Fattah, Z. A., Gingras, M. K., Caldwell, M. W., & Pemberton, G. S. (2010). Sedimentary environments and depositional characteristics of the middle to upper Eocene whale-bearing succession in the Fayum depression Egypt. *Sedimentology, 57*(2), 446–476.

Ahmed, M., & Abdelmohsen, K. (2018). Quantifying modern recharge and depletion rates of the Nubian Aquifer in Egypt. *Surveys in Geophysics, 39*(4), 729–751.

Alisiobi, A. R., & Ako, B. D. (2012). Groundwater investigation using combined geophysical methods. AAPG Annual Convention and Exhibition, Long Beach, California Search and Discovery, Article 40914.

Altamimi, Z., Métivier, L., Rebischung, P., Rouby, H., & Collilieux, X. (2017). ITRF2014 Plate Motion Model. *Geophysical Journal International, 209*(3), 1906–1912. https://doi.org/10.1093/gji/ggx136

Aly, N., Hamed, A., & Abd El-Al, A. (2020). The impact of hydric swelling on the mechanical behavior of Egyptian Helwan limestone. *Periodica Polytechnica Civil Engineering, 64*(2), 589–596.

Anan, T., & El Shahat, A. (2014). Provenance and sequence architecture of the middle-late Eocene Gehannam and Birket Qarun formations at Wadi Al hitan, Fayum province Egypt. *Journal of African Earth Sciences, 100*, 614–625.

Araffa, S. A., Abdelazeem, M., Sabet, H. S., & Dabour, A. M. A. (2021). Hydrogeophysical investigation at El Moghra Area, North Western Desert. *Egypt. Environmental Earth Sciences, 80*(2), 1–17.

Ariyo, S. O., Folorunso, A. F., & Ajibade, O. M. (2011). Geological and geophysical evaluation of the Ajana area's groundwater potential, southwestern Nigeria. *Earth Science Research Journal, 15*(1), 35–40.

Azmy, E., Araffa, S., & Helaly, A. (2021). Geophysical interpretation for delineating groundwater and subsurface structure in the East of Cairo City Egypt. *Pure and Applied Geophysics, 178*(8), 3619–3635. https://doi.org/10.1007/s00024-021-02748-7

Beadnell, H.J.L. (1905). The topography and geology of the Fayum Province of Egypt. Surv. Dep. 101.

Bosworth, W., El-Hawat, A. S., Helgeson, D. A., & Burke, K. (2008). Cyrenaican "shock absorber" and associated inversion strain shadow in the collision zone of Northeast Africa. *Geology, 36*, 695–698.

Bown, T. M., & Kraus, M. J. (1988). Geology and paleoenvironment of the Oligocene Jebel El Qatrani Formation and adjacent rocks, Fayum depression, Egypt. *U.S Geol. Surv. Prof. Pap., 1452*, 1–60.

CONCO/EGPC. (1987). Geological map of Egypt, Scale 1:500,000. CONCO with cooperation of The Egyptian General Petroleum Corporation.

Dach, R., Hugentobler, U., Fridez, P., & Meindl, M. (2007). *Bernese GNSS Software Version 52*. Bern: Astronomical Institute, University of Bern.

Deep, Mohamed A.L., Araffa, Sultan Awad Sultan., Mansour, Salah A., Taha, Ayman I., Mohamed, Ahmed, & Othman, Abdullah. (2021). Geophysics and remote sensing applications for groundwater exploration in fractured basement: A case study from Abha area, Saudi Arabia. *Journal of African Earth Sciences, 184*, 104368. https://doi.org/10.1016/j.jafrearsci.2021.104368

El-Fawal, F. M., El-Asmar, H. M., & Sarhan, M.A.E.-F. (2013). Depositional evolution of the middle-upper Eocene rocks, Fayum area Egypt. *Arabian Journal of Geosciences, 6*, 749–760.

El-Sayed, M.A., Mabrouk, M.A. (1991). Geomorphology of the Nile during the Quaternary from the electrical survey at Beni-Suef, Egypt. Egyptian Geophysical Society Proceedings 8th Annual Meeting, 215.

Getech. (1992). The African Magnetic Mapping Project. Commercial Report (unpublished).

Gingerich, P. D. (1993). Oligocene age of the Gebel Qatrani Formation, Fayum Egypt. *Journal of Human Evolution, 24*, 207–218.

Guiraud, R., & Bosworth, W. (1999). Phanerozoic geodynamic evolution of northeastern Africa and the northwestern Arabian platform. *Tectonophysics, 315*, 73–108.

Interpex., 2008Interpex. (2008). IX1D V3 Instruction Manual. Golden, CO, USA: Interpex Ltd

Issawi, B., Francis, M., Youssef, A., & Osman, R. (2009). The Phanerozoic of Egypt: A geodynamic approach. *Geological Survey of Egypt, 81*, 1–589.

Khalil, Ahmed, Abdel, Tharwat H., Hafeez, Ahmed El, Kotb, HS Saleh., Mohamed, Waheed H., & Takla, E. M. (2022). Subsurface Structural Characterization as Deduced from Potential Field Data-West Beni Suef, Western Desert Egypt. *Arabian Journal of Geosciences, 15*(1), 1–15. https://doi.org/10.1007/s12517-022-10900-1

King, C., Underwood, C., & Steurbaut, E. (2014). Eocene stratigraphy of the Wadi Al Hitan world heritage site and adjacent areas (Fayum, Egypt). *Stratigraphy, 11*, 185–234.

Lotfy, H., & Van der Voo, R. (2007). Tropical northeast Africa in the middle-late Eocene: Paleomagnetism of the marine-mammals sites and basalts in the Fayum province Egypt. *Journal of African Earth Sciences, 47*, 135–152.

Mohamed, Ahmed. (2020). Gravity applications to groundwater storage variations of the Nile Delta Aquifer. *Journal of Applied Geophysics, 182*, 104177. https://doi.org/10.1016/j.jappgeo.2020.104177

Mohamed, M., Fathy, A., & Ayman, I. (2021). Hydrogeophysical Study of Sub-Basaltic Alluvial Aquifer in the Southern Part of Al-Madinah Al-Munawarah. *Saudi Arabia Sustainability, 13*, 9841. https://doi.org/10.3390/su13179841

Moustafa, A. R. (2008). Mesozoic-Cenozoic basin evolution in the northern Western Desert of Egypt. *Geology of East Libya, 3*, 29–46.

Olorunfermi, M. O., Ojo, J. S., & Akintunde, O. M. (1999). Hydrogeophysical evaluation of the groundwater potentials of the Akure Metropolis, southwestern Nigeria. *Journal of Mining and Geology, 35*, 201–228.

RIGW/IWACO (1989). Development and management of groundwater resources in the Nile Valley and Delta: Assessment of groundwater pollution from domestic activities. Kanater El-Khairia, Egypt: Research Inst, For Groundwater.

RIGW (1997). Hydrogeological Map of Egypt, Scale 1: 500000, Beni Suef Map Sheet.

RIGW, IWACO (1998). Environmental Management of Groundwater Resources (EMGR), Identification, Priority Setting and Selection of Area for Monitoring Groundwater Quality. Technical Report TN/70.00067/WQM/97/20, Res. Instit. for Groundwater (RIGW), Egypt.

Said, R. (1990). The Geology of Egypt. Balkema, p. 734.

Said, R. (1962). *The Geology of Egypt* (p. 377). Elsevier.

Shehata, A. A., El Fawal, F. M., Ito, M., Aal, M. H. A., & Sarhan, M. A. (2018). Sequence stratigraphic evolution of the syn-rift Early Cretaceous sediments, West Beni-Suef Basin, the Western Desert of Egypt with remarks on its hydrocarbon accumulations. *Arabian Journal of Geosciences, 11*, 331.

Shen, D. (2015). Environmental sustainability and economic development: A world view. *Journal of Economics and Sustainable Development, 6*(6), 51–59.

Taha, A. I., Deep, M. A., & Mohamed, A. (2021). Investigation of groundwater occurrence using gravity and electrical resistivity methods: A case study from Wadi Sar, Hijaz Mountains Saudi Arabia. *Arabian Journal of Geosciences, 14*(1), 1–17. https://doi.org/10.1007/s12517-021-06628-z

Vondra, C. F. (1974). Upper Eocene transitional and near shore marine Qasr El-Sagha Formation. *Fayium Depression, 4*, 79–94.

Zalat, A. (1995). Calcareous nannoplakton and diatoms from the Eocene/Pliocene sediments, Fayoum depression Egypt. *Journal of African Earth Sciences, 20*, 227–244.